

# Competing effects of inertia, sheet elasticity, and fluid viscoelasticity on the synchronization of two actuated sheets

Chaojie Mo and Dmitry A. Fedosov\*

*Theoretical Physics of Living Matter, Institute of Biological Information Processing and Institute for Advanced Simulation, Forschungszentrum Jülich, 52425 Jülich, Germany*

(Dated: September 17, 2020)

Synchronization of two actuated sheets serves as a simple model for the interaction between flagellated microswimmers. Various factors, including inertia, sheet elasticity, and fluid viscoelasticity, have been suggested to facilitate the synchronization of two sheets; however, the importance of different contributions to this process still remains unclear. We perform a systematic investigation of competing effects of inertia, sheet elasticity, and fluid viscoelasticity on the synchronization of two sheets. Characteristic time  $\tau^s$  for the synchronization caused by inertial effects is inversely proportional to sheet Reynolds number  $Re$ , such that  $\tau^s \omega \propto Re^{-1}$  with  $\omega$  being the wave frequency. Synchronization toward stable in-phase or opposite-phase configuration of two sheets is determined by the competition of inertial effects, sheet elasticity, fluid compressibility and viscoelasticity. Interestingly, fluid viscoelasticity results in strong synchronization forces for large beating amplitudes and Deborah numbers  $De > 1$ , which dominates over other factors and favors the in-phase configuration. Therefore, our results show that fluid viscoelasticity can dramatically enhance synchronization of microswimmers. Our investigation deciphers the importance of different competing effects for the synchronization of two actuated sheets, leading to a better understanding of interactions between microswimmers and their collective behavior.

## I. INTRODUCTION

Locomotion of biological and artificial microswimmers and their collective behavior have attracted considerable scientific and technological attention recently [1–4]. The foci of such studies range from physical mechanisms governing the motion and interaction of microswimmers to their use in practical applications and the emergence of collective behavior. One of the interesting aspects is the interaction between multiple swimmers facilitated by a suspending fluid medium. For instance, swimming spermatozoa tend to synchronize their beating flagella when they are close to each other [5–7]. Even though distinct spermatozoa likely have differences in their intrinsic properties, they are able to adjust their beating characteristics (e.g., phase and frequency), and swim together as a concerted unit [5]. Furthermore, synchronization of motion mediated by suspending medium is relevant for many other microswimmers, which propel using helical flagella [8, 9] or cilia [10, 11].

One of the first propositions that the synchronization of microswimmers is mediated by hydrodynamic interactions corresponds to the theoretical work of Taylor in 1951 [12] for two waving tails. Interestingly, the first experimental confirmation of the importance of hydrodynamic interactions for the synchronization of two beating flagella has been realized only a few years ago [13]. Theoretical analysis of microswimmer behavior and possible synchronization interactions is generally performed under the assumption of zero Reynolds number (i.e., no inertia) [1, 12, 14, 15], because of non-linearity of the inertial term in the Navier-Stokes equations. Several theoretical studies have also considered the effect of fluid inertia at small Reynolds numbers [16, 17]. Even though the assumption of vanishing inertia is generally justified by the small size and low swimming velocity of microswimmers, there are examples of artificial microrobots which operate at non-negligible Reynolds numbers [4, 18, 19]. A theory, in which the synchronization of two inextensible waving sheets is considered, predicts no synchronization of the sheets having a front-back motion symmetry (e.g., a pure sine wave) due to kinematic reversibility of Stokes flow (i.e., under the assumption of no inertia) [20]. Thus, synchronization is only possible if there exist additional irreversible factors which break the symmetry [20, 21]. For example, to make the synchronization of two sheets possible, a front-back asymmetry in the beating motion is proposed [20, 22]. Furthermore, other factors, such as non-negligible inertia [23–25], sheet elasticity [26], and viscoelasticity of non-Newtonian fluids [27, 28], are sufficient to break the symmetry and enable synchronization.

Another interesting aspect in the synchronization of two sheets is that there exist two stable synchronized configurations, namely in-phase and opposite-phase conformations with a phase difference  $\phi_d = 0$  and  $\phi_d = \pi$  between the two sheets, respectively. Either the in-phase or opposite-phase configuration is stable, depending on various conditions. For instance, the geometry of a prescribed asymmetric wave determines the preference for each configuration [20, 22].

---

\* d.fedosov@fz-juelich.de

In case of non-negligible inertial effects, the opposite-phase conformation is preferred with increasing Reynolds number [23]. Sheet flexibility [26] as well as viscoelasticity of an Oldroyd-B fluid [27, 28] drive the system toward the in-phase configuration. Noteworthy, the theory of sheet synchronization in Oldroyd-B fluids predicts the strongest synchronization force at Deborah number  $De$  of unity, while at large  $De$ , the synchronization forces asymptotically approach zero. For comparison, Deborah number of a swimming sperm in cervical mucus is larger than 100, and fluid viscoelasticity dramatically enhances clustering of bovine sperm [29]. Despite several existing studies on sheet synchronization, the interplay and importance of different competing effects remains unclear.

We perform a systematic analysis of the importance of different aforementioned factors for the synchronization of two sheets. Our simulations are based on the smoothed dissipative particle dynamics (SDPD) method [30–32], a particle-based hydrodynamics technique, where both Newtonian and Oldroyd-B fluids are implemented. Two different setups are considered, including (i) a pair of inextensible waving sheets with a prescribed motion, for which synchronization forces are measured, and (ii) two flexible sheets with an internal actuation, for which dynamic synchronization toward one of the stable configurations is simulated. Our results show that for any non-zero Reynolds number  $Re$ , the two sheets always synchronize regardless of its magnitude. When inertial effects dominate, the opposite-phase configuration is preferred and a characteristic time  $\tau^s$  for the synchronization normalized by the wave frequency  $\omega$  is inversely proportional to  $Re$ , i.e.  $\tau^s \omega \propto Re^{-1}$ .

Sheet elasticity also affects stable synchronized configuration, driving the two sheets toward the in-phase configuration. Fluid viscoelasticity, when a dominating factor, also drives the sheets toward the in-phase configuration. Nevertheless, at high enough  $Re$ , inertial effects may favor the opposite-phase conformation even in viscoelastic fluids. The modes of stable synchronized configurations with respect to different factors are summarized in Table II. Furthermore, note that the failure of the theory in Ref. [27] to predict large synchronization forces at  $De > 1$  is related to the leading order approximation in terms of the wave amplitude. For large enough wave amplitudes, strong deviations in synchronization forces with respect to the theoretical predictions are observed for  $De > 1$ , leading to a dramatic enhancement of sheet synchronization by fluid viscoelasticity. These results are consistent with experimental observations of the pronounced enhancement of sperm clustering in viscoelastic fluids [29]. In conclusion, our results provide better understanding of different competing effects for sheet synchronization and can be used to control the synchronization of artificial swimmers.

The paper is organized as follows. Section II presents fluid and sheet models, simulation setup, and the validation of these models against available theoretical predictions. In section III A, synchronization of two sheets in Newtonian fluids is studied for different model parameters affecting the value of  $Re$ , fluid compressibility, and sheet flexural rigidity. Section III B presents synchronization results in Oldroyd-B viscoelastic fluids. Swimming efficiency of two synchronized sheets is discussed in section III C. Finally, we conclude in section IV.

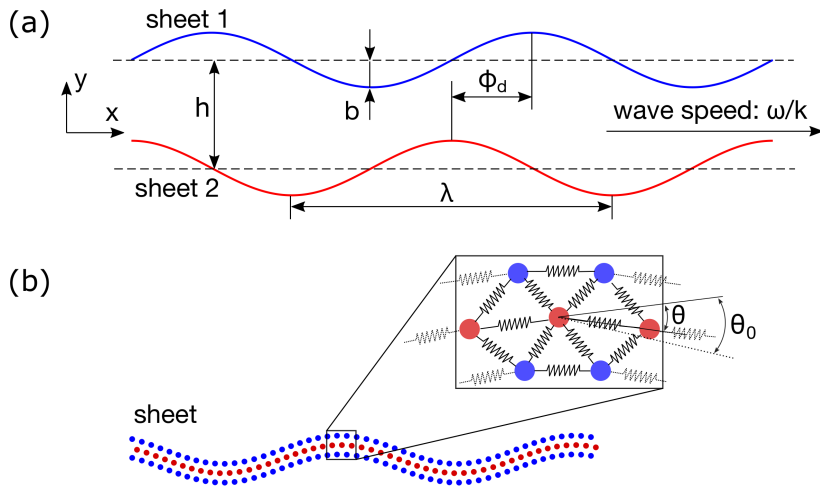


FIG. 1. Model schematic. (a) Setup and basic parameters of the two actuated sheets. Here,  $b$  is the wave amplitude,  $k$  is the wave number,  $\lambda = 2\pi/k$  is the wave length,  $\omega$  is the wave frequency, such that the wave speed is  $\omega/k$ .  $h$  is the distance between average positions of the sheets and  $\phi_d$  is a phase difference between their actuations. (b) Model representation of a flexible sheet constructed by three particle layers interconnected by springs.  $\theta$  is the instantaneous angle between two adjacent springs in the middle layer (marked in red), and  $\theta_0$  is the spontaneous angle employed for sheet actuation.

## II. METHODS AND MODELS

### A. Viscoelastic fluid model

Fluid flow is modeled by the smoothed dissipative particle dynamics (SDPD) method [30, 31], which is a particle-based mesoscopic hydrodynamics approach. SDPD is derived through a Lagrangian discretization of the Navier-Stokes equations similar to the smoothed particle hydrodynamics (SPH) method [33], with the proper inclusion of thermal fluctuations following the dissipative particle dynamics (DPD) approach [34, 35]. We employ an SDPD version which conserves angular momentum [31], as it can be crucial for some problems [36, 37]. In SDPD, each particle can be considered as a small fluid volume (or Lagrangian discretization point) characterized by a position  $\mathbf{r}_i$ , velocity  $\mathbf{v}_i$ , and mass  $m_i$ . In addition, each SDPD particle possesses a spin angular velocity  $\boldsymbol{\psi}_i$  and moment of inertia  $I_i$  introduced for the enforcement of angular momentum conservation [31].

SDPD particles  $i$  and  $j$  interact through four pairwise forces, including conservative  $\mathbf{F}_{ij}^C$ , dissipative  $\mathbf{F}_{ij}^D$ , rotational  $\mathbf{F}_{ij}^R$ , and random  $\tilde{\mathbf{F}}_{ij}$  forces given by

$$\begin{aligned}\mathbf{F}_{ij}^C &= \left( \frac{\boldsymbol{\Pi}_i}{d_i^2} + \frac{\boldsymbol{\Pi}_j}{d_j^2} \right) F_{ij} \cdot \mathbf{r}_{ij}, \\ \mathbf{F}_{ij}^D &= -\gamma_{ij} [\mathbf{v}_{ij} + (\mathbf{e}_{ij} \cdot \mathbf{v}_{ij}) \mathbf{e}_{ij}], \\ \mathbf{F}_{ij}^R &= -\gamma_{ij} \frac{\mathbf{r}_{ij}}{2} \times (\boldsymbol{\psi}_i + \boldsymbol{\psi}_j), \\ \tilde{\mathbf{F}}_{ij} &= \sigma_{ij} \left( d\overline{\mathcal{W}}_{ij}^s + \frac{1}{3} \text{tr}[d\mathcal{W}_{ij}] \mathbf{1} \right) \cdot \frac{\mathbf{e}_{ij}}{dt},\end{aligned}\tag{1}$$

where  $\mathbf{r}_{ij} = \mathbf{r}_i - \mathbf{r}_j$ ,  $\mathbf{v}_{ij} = \mathbf{v}_i - \mathbf{v}_j$ , and  $\mathbf{e}_{ij} = \mathbf{r}_{ij}/r_{ij}$ . Particle number density  $d_i$  is computed as  $d_i = \sum_j W_{ij}$  using a smoothing kernel function  $W_{ij} = W(r_{ij})$  that vanishes beyond a cutoff radius  $r_c$  and defines a non-negative function  $F_{ij}$  through the equation  $\nabla_i W_{ij} = -\mathbf{r}_{ij} F_{ij}$ . Then, particle mass density is given by  $\rho_i = m_i d_0$ . In the SDPD formulation for Newtonian fluids, the stress tensor  $\boldsymbol{\Pi}_i = p_i^s \mathbf{1}$  contains only diagonal (i.e. pressure) components. The pressure  $p_i^s$  is determined by the equation of state (EoS)  $p_i^s = p_0 (d_i/d_0)^\nu - p_b$ , where  $d_0$  is the average number density, and  $p_0$ ,  $\nu$ , and  $p_b$  are freely selected parameters. Furthermore,  $\gamma_{ij}$  and  $\sigma_{ij}$  are the corresponding force amplitudes

$$\gamma_{ij} = \frac{20\eta}{7} \frac{F_{ij}}{d_i d_j}, \quad \sigma_{ij} = 2\sqrt{k_B T \gamma_{ij}},\tag{2}$$

where  $\eta$  is the fluid dynamic viscosity and  $T$  is the equilibrium temperature. Eq. (1) also contains a matrix of independent Wiener increments  $d\mathcal{W}_{ij}$  with its trace  $\text{tr}[d\mathcal{W}_{ij}]$  and the traceless symmetric part  $d\overline{\mathcal{W}}_{ij}^s = \frac{1}{2} (d\mathcal{W}_{ij} + d\mathcal{W}_{ji}) - \frac{1}{3} \text{tr}[d\mathcal{W}_{ij}]$ , and the time step  $dt$ .

The evolution of particle positions, translational and angular velocities is obtained by integration of the following equations of motion

$$\begin{aligned}\dot{\mathbf{r}}_i &= \mathbf{v}_i, \\ m_i \dot{\mathbf{v}}_i &= \sum_j \mathbf{F}_{ij} = \sum_j (\mathbf{F}_{ij}^C + \mathbf{F}_{ij}^D + \mathbf{F}_{ij}^R + \tilde{\mathbf{F}}_{ij}), \\ \dot{\boldsymbol{\psi}}_i &= \frac{1}{2I_i} \sum_j \mathbf{r}_{ij} \times \mathbf{F}_{ij},\end{aligned}\tag{3}$$

using the velocity-Verlet algorithm [38].

Fluid elasticity is introduced following the idea that every fluid particle contains  $N_p$  bead-spring dumbbells [32]. Dumbbells are not explicitly modeled, but represented by a conformation tensor  $\mathbf{c}$  that characterizes their stretching state within each particle. The conformation tensor is expressed as  $\mathbf{c}_i = 1/N_p \sum_a^{N_p} \mathbf{q}_a \mathbf{q}_a$ , where  $\mathbf{q}_a$  is the end-to-end distance of the  $a$ -th dumbbell within a fluid particle  $i$ . Then, the stress tensor  $\boldsymbol{\Pi}_i$  in Eq. (1) is modified by the addition of  $\mathbf{c}$  contribution as follows [32]

$$\boldsymbol{\Pi}_i = p_i^s \mathbf{1} + N_p d_i k_B T (\mathbf{1} - \mathbf{c}_i).\tag{4}$$

Evolution of the conformation tensor proceeds according to [32]

$$\dot{\mathbf{c}}_i^{\mu\mu'} = \frac{1}{d_i} \mathbf{c}_i^{\mu\nu} \boldsymbol{\kappa}_i^{\nu\mu'} + \frac{1}{d_i} \mathbf{c}_i^{\mu'\nu} \boldsymbol{\kappa}_i^{\nu\mu} + \frac{1}{\tau} (\delta^{\mu\mu'} - \mathbf{c}_i^{\mu\mu'}) + \frac{d\tilde{\mathbf{c}}_i^{\mu\mu'}}{dt},\tag{5}$$

where  $\kappa_i^{\mu\nu} = \sum_j F_{ij} r_{ij}^\mu v_{ij}^\nu$  is the velocity gradient tensor,  $\tau$  is the dumbbell relaxation time, and  $d\tilde{c}$  is the noise term. This model corresponds to the well-known viscoelastic Oldroyd-B model, in which the total fluid viscosity  $\eta = \eta_s + \eta_p$  has two contributions, including solvent  $\eta_s$  and polymer  $\eta_p$  components. The polymer contribution is given by  $\eta_p = k_B T d_0 N_p \tau$ , and can easily be adjusted through the parameters  $N_p$  and  $\tau$ .

In this work, the smoothing kernel is represented by the two dimensional (2D) Lucy function [39]

$$W(r) = \frac{5}{\pi r_c^2} \left(1 + 3 \frac{r}{r_c}\right) \left(1 - \frac{r}{r_c}\right)^3. \quad (6)$$

Thermal fluctuations are neglected by setting  $k_B T = 10^{-6}$ , such that the SDPD method is essentially reduced to SPH. Furthermore, we also neglect the noise term of the conformation tensor, i.e.  $d\tilde{c} = 0$ .

## B. Sheet model and simulation setup

Figure 1(a) shows a schematic of our 2D simulation setup with two sheets. According to the theoretical work of Taylor [12], traveling wave  $y(x, t) = b \sin(kx - \omega t + \phi)$  on an inextensible 2D sheet can be modeled through the imposition of particle velocities as

$$\begin{aligned} v_x &= \frac{\omega}{k} - Q \cos \theta, & v_y &= -Q \sin \theta, \\ \tan \theta &= bk \cos(kx - \omega t + \phi), & Q &= \frac{\omega}{2\pi k} \int_0^{2\pi} (1 + b^2 k^2 \cos^2 \xi)^{1/2} d\xi, \end{aligned} \quad (7)$$

where  $b$  is the wave amplitude,  $k$  is the wave number related to the wave length  $\lambda = 2\pi/k$ ,  $\omega$  is the wave angular frequency, and  $\phi$  is the phase shift. Even though this traveling wave propagates with a wave speed  $\omega/k$ , material points of the sheet do not move forward or backward on average, and thus they represent a waving (rather than swimming) sheet, which will be referred to as *prescribed actuation* further in text. However, such sheet actuation generates a far-field flow [12], which can result in non-zero hydrodynamic synchronization forces between two waving sheets.

The prescribed actuation strategy in Eq. (7) cannot be used to model dynamic synchronization of two swimming sheets. Furthermore, it does not account for a possible flexural rigidity of the sheets. Model of a flexible sheet is shown in Fig. 1(b), where three layers of sheet particles are interconnected by harmonic springs. The spring potential is given by

$$U(l) = \frac{\zeta_s}{2} (l - l_0)^2, \quad (8)$$

where  $\zeta_s$  is the spring stiffness,  $l$  is its length, and  $l_0$  is the equilibrium spring length. Actuation of the flexible sheets is performed using the middle layer (marked red in Fig. 1(b)), where a harmonic angle potential

$$U(\theta) = \frac{\zeta_\theta}{2} (\theta - \theta_0)^2 \quad (9)$$

is implemented for each pair of adjacent springs. Here,  $\zeta_\theta$  is the potential strength,  $\theta$  is the instantaneous angle between two adjacent springs in the middle layer, and  $\theta_0$  is the spontaneous angle. A traveling wave on the sheets is imposed by the varying  $\theta_0(x, t) = \theta_b \sin(kx_s - \omega t)$ , where  $\theta_b$  is the angle amplitude and  $x_s = il_0$  is the distance along the sheet with  $i$  representing particle numbering along the middle layer. Flexural rigidity  $\kappa$  of this model can be estimated as  $\kappa = 2\zeta_s l_0^3 + \zeta_\theta l_0$  (see Appendix). In addition to the parameters  $\zeta_\theta$  and  $\theta_b$ , the actual wave amplitude in this case is affected by the sheet flexural rigidity, wave frequency, and fluid viscoelasticity. This model of sheet motion will be referred to as *internal actuation*, and allows the simulation of dynamic synchronization of two swimming sheets. To constrain sheet motion in the  $y$  direction, a tether force  $\mathbf{F}_{\text{teth}} = -\zeta_{\text{teth}}(y_{\text{cm}} - y_0)\mathbf{e}_y$  is applied uniformly to all sheet particles, where  $\zeta_{\text{teth}}$  is the spring stiffness,  $y_{\text{cm}}$  is the center-of-mass position of the sheet, and  $y_0$  is the preferred position along the  $y$  axis. Since simulation domain is periodic, any rotation of the sheet would necessarily result in its stretching, and therefore, its average direction along the  $x$  axis is self constrained.

In simulations, two sheets separated by the distance  $h$  between their average positions are embedded into the modeled SDPD fluid. Each sheet is constructed by three layers of particles and is driven either through the prescribed actuation [see Eq. (7)] or by internal actuation [see Eq. (9)]. The number density of sheet particles is the same as that of fluid particles. Therefore, interactions between fluid and sheet particles are identical to the fluid-fluid interactions. The simulation domain  $L_x \times L_y$  is periodic in both dimensions. The cutoff radius is fixed at  $r_c = 1.6$

TABLE I. Parameters used in simulations.

| Parameters  | Values  |
|---|---|
| Cutoff radius $r_c$                                       | 1.6   |
| Reference mass density $\rho_{\text{ref}}$                | 6.25  |
| Reference dynamic viscosity $\eta_{\text{ref}}$           | 6.25  |
| Energy unit $k_B T$                                       | 1e-6  |
| Size of the simulation domain $L_x \times L_y$            | $12.5r_c \times 18.75r_c$                     |
| Wave number $k$   | $4\pi/L_x$                                    |
| Number density $d_0$                                      | $16/r_c^2$                                    |
| Time unit $t_{\text{ref}}$                                | $r_c^2 \rho_{\text{ref}} / \eta_{\text{ref}}$ |
| Force unit $F_{\text{ref}}$                               | $r_c^3 \rho_{\text{ref}} / t_{\text{ref}}^2$  |
| Pressure unit $p_{\text{ref}}$                            | $r_c^2 \rho_{\text{ref}} / t_{\text{ref}}^2$  |
| Spring stiffness unit $\zeta_{\text{ref}}$                | $r_c^2 \rho_{\text{ref}} / t_{\text{ref}}^2$  |
| Angle potential strength unit $\zeta_{\text{ref}}^\theta$ | $r_c^4 \rho_{\text{ref}} / t_{\text{ref}}^2$  |
| Flexural rigidity unit $\kappa_{\text{ref}}$              | $r_c^5 \rho_{\text{ref}} / t_{\text{ref}}^2$  |
| Average distance between the two sheets $h$               | $2.875r_c$                                    |
| Stiffness of the tether spring $\zeta_{\text{teth}}$      | $8192\zeta_{\text{ref}}$                      |
| Angle potential strength $\zeta_\theta$                   | $640\zeta_{\text{ref}}^\theta$                |
| Difference in pressure coefficients $p_0 - p_b$           | $32.8p_{\text{ref}}$                          |

in all simulations and will be used as a basic length scale. Also, fluid resolution characterized by the number density  $d_0 = 16/r_c^2$  is kept the same in all simulations. Furthermore, we introduce reference mass density  $\rho_{\text{ref}} = 6.25$  and dynamic viscosity  $\eta_{\text{ref}} = 6.25$ , which define a mass scale  $m_{\text{ref}} = \rho_{\text{ref}} r_c^2$  and a time scale  $t_{\text{ref}} = r_c^2 \rho_{\text{ref}} / \eta_{\text{ref}}$ . We also define  $F_{\text{ref}} = r_c^3 \rho_{\text{ref}} / t_{\text{ref}}^2$ ,  $p_{\text{ref}} = r_c^2 \rho_{\text{ref}} / t_{\text{ref}}^2$ ,  $\zeta_{\text{ref}} = r_c^2 \rho_{\text{ref}} / t_{\text{ref}}^2$ ,  $\zeta_{\text{ref}}^\theta = r_c^4 \rho_{\text{ref}} / t_{\text{ref}}^2$ ,  $\kappa_{\text{ref}} = r_c^5 \rho_{\text{ref}} / t_{\text{ref}}^2$  for scaling force, pressure, spring stiffness, angle potential strength, and flexural rigidity units, respectively. Simulation parameters are summarized in Table I or otherwise specified explicitly in text.

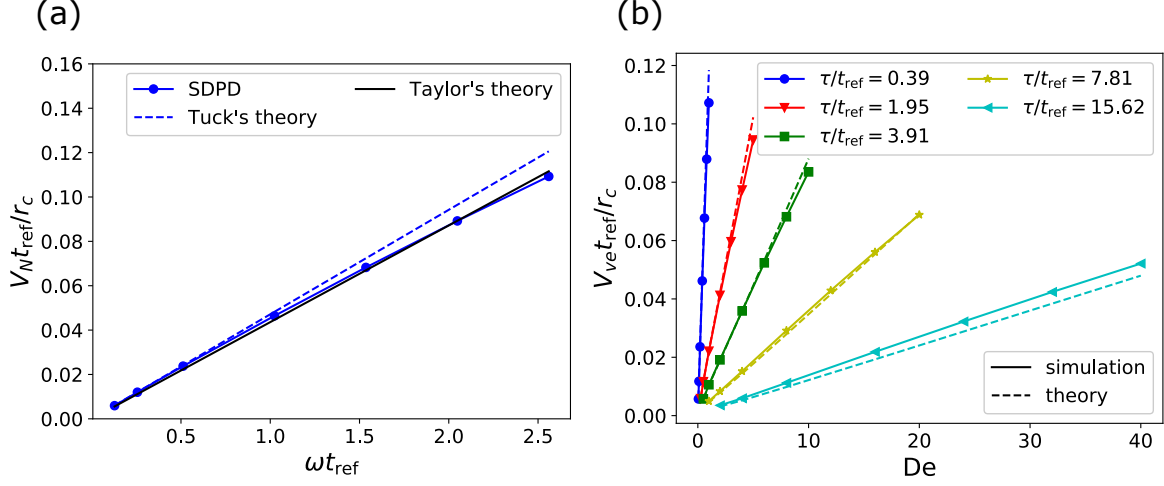


FIG. 2. Model validation. (a) Far-field velocity  $V_N$  generated by a single waving sheet in a Newtonian fluid in comparison with the theoretical prediction by Taylor [12] for  $\text{Re} = 0$  [Eq. (10)] and by Tuck [17] for  $\text{Re} > 0$ . Here,  $\eta/\eta_{\text{ref}} = 64$ . (b) Comparison of simulated and theoretical far-field velocities  $V_{ve}$  generated by a waving sheet in viscoelastic fluids with various relaxation times  $\tau$ . The theoretical predictions correspond to Eq. (11). Here,  $N_p = 3 \times 10^6$  and  $\eta_s/\eta_{\text{ref}} = 64$ . In all simulations,  $L_x \times L_y = 18.75r_c \times 31.25r_c$ ,  $b/r_c = 0.375$ ,  $\rho/\rho_{\text{ref}} = 1$ ,  $p_0/p_{\text{ref}} = 409.6$ , and  $\nu = 7$ .

### C. Model validation

Since our SDPD formulation is practically reduced to SPH by neglecting random terms, we can take advantage of rich SPH literature for the method validation. For instance, a similar SPH formulation has been used to simulate different fluid flows at low and moderate  $Re$  [40, 41], in good agreement with the corresponding analytical and/or finite-element results. Note that SPH may become unstable at high  $Re$  [42]. To verify the correctness of SDPD implementation for Newtonian fluids, wall-bounded Poiseuille flow and unsteady flow above an oscillating plate (or Stokes second problem) were simulated, showing an excellent agreement with the corresponding analytical solutions. The viscoelastic Oldroyd-B model has also been validated using unsteady Kolmogorov flow [32].

In the context of swimming sheets, we revisit the problem of a single waving sheet both in Newtonian and viscoelastic fluids. An inextensible 2D sheet actuated according to Eq. (7) generates a far-field flow velocity  $V_N$  in the  $x$  direction. The theoretical prediction of  $V_N$  is given by [12]

$$V_N = \frac{1}{2}\omega b^2 k \left(1 - \frac{19}{16}b^2 k^2\right). \quad (10)$$

Figure 2(a) compares simulation results for  $V_N$  in a Newtonian fluid with the theoretical prediction in Eq. (10), demonstrating an excellent agreement. Here,  $Re = 8.95 \times 10^{-4}$ , defined as  $Re = fb^2\rho/\eta$  with  $f = \omega/(2\pi)$ , is small enough and can be neglected. The theoretical result by Tuck [17] for  $Re > 0$  is also shown in Fig. 2(a); however, it is only of the order  $\mathcal{O}(b^2k^2)$  and is therefore less accurate.

For viscoelastic Oldroyd-B fluids, a theoretical prediction for the far-field velocity  $V_{ve}$  generated by a waving sheet is given by [43]

$$V_{ve} = \frac{1}{2}\omega b^2 k \frac{1 + De^2\eta_s/\eta}{1 + De^2}, \quad (11)$$

where  $\eta_s$  is the solvent component of viscosity and  $De = \tau\omega$  is the Deborah number that represents a ratio of relaxation time to the characteristic time of sheet motion. Figure 2(b) shows the comparison of simulated  $V_{ve}$  for a waving sheet in various viscoelastic fluids against the analytical predictions in Eq. (11) as a function of  $De$ . The simulation results (solid lines) for various  $\tau$  agree well with the analytical predictions (dashed lines). A small deviation mainly results from a slight shear dependence of SDPD fluid viscosity.

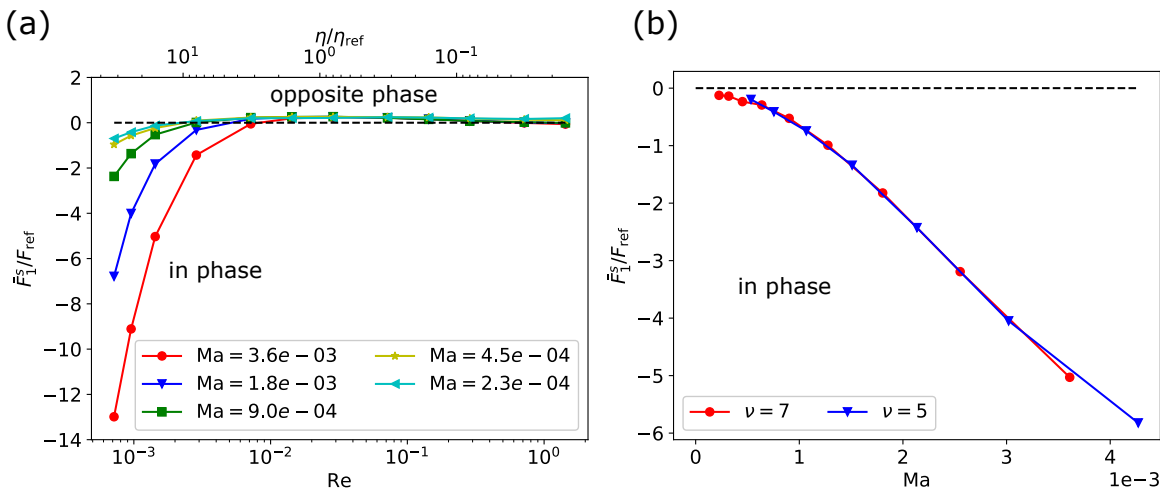


FIG. 3. Synchronization force amplitudes of two waving sheets with prescribed actuation for different  $Re$  and  $Ma$  numbers in a Newtonian fluid. (a)  $\bar{F}_1^s$  as a function of  $Re$  (fluid viscosity  $\eta$  is varied) for various  $Ma$  values and  $\nu = 7$ . (b)  $\bar{F}_1^s$  as a function of  $Ma$  (the pressure parameter  $p_0$  is varied) for  $\nu = 5$  and  $\nu = 7$ . Here,  $\eta/\eta_{ref} = 16$  and  $Re \approx 1.4 \times 10^{-3}$ . Note that  $\bar{F}_1^s$  corresponds to the first sheet, while  $\bar{F}_2^s = -\bar{F}_1^s$ . In all cases,  $\omega t_{ref} = 1.024$ ,  $b/r_c = 0.375$ , and  $\rho/\rho_{ref} = 1$ .

### III. RESULTS AND DISCUSSION

We investigate the synchronization of two sheets, and in particular, its dependence on inertial effects, fluid compressibility, sheet flexural rigidity, and fluid viscoelastic properties. Two sheets placed side by side with a distance  $h$

apart (see Fig. 1) can have a phase difference in their motion given by  $\phi_d = \phi_2 - \phi_1$ . Generally, the synchronization force in the  $x$  direction is a function of  $\phi_d$  and has a functional form [26, 27]

$$F^s(\phi_d) = \bar{F}^s \sin(\phi_d), \quad (12)$$

where  $\bar{F}^s$  is the force amplitude. The synchronization forces on the two sheets have the same magnitude, but different signs, which means that they act in opposite directions. For the calculation of force amplitude  $\bar{F}^s$ , several simulations for different  $\phi_d$  values in the interval  $[0, \pi]$  (with an increment of  $\pi/30$  for simulations with Newtonian fluids and of  $\pi/15$  for simulations with Oldroyd-B fluids) are performed, and the resultant force data are fitted using Eq. (12). Note that the force amplitude  $\bar{F}^s$  can also be negative, as the fitting is carried out within the range  $[0, \pi]$ .

There exist two possible synchronized configurations:

- (i)  $\phi_d = 0$  – an in-phase configuration,
- (ii)  $\phi_d = \pi$  – an opposite-phase configuration.

Due to our definition of the phase difference as  $\phi_d = \phi_2 - \phi_1$ , the synchronization forces  $F_1^s(\phi_d) = -F_2^s(\phi_d) < 0$  drive the sheets toward the in-phase configuration with  $\phi_d = 0$ , while for  $F_1^s(\phi_d) = -F_2^s(\phi_d) > 0$ , the opposite-phase conformation with  $\phi_d = \pi$  is stable. Further, simulation results will mainly be presented in terms of  $\bar{F}_1^s$  for the first sheet only.

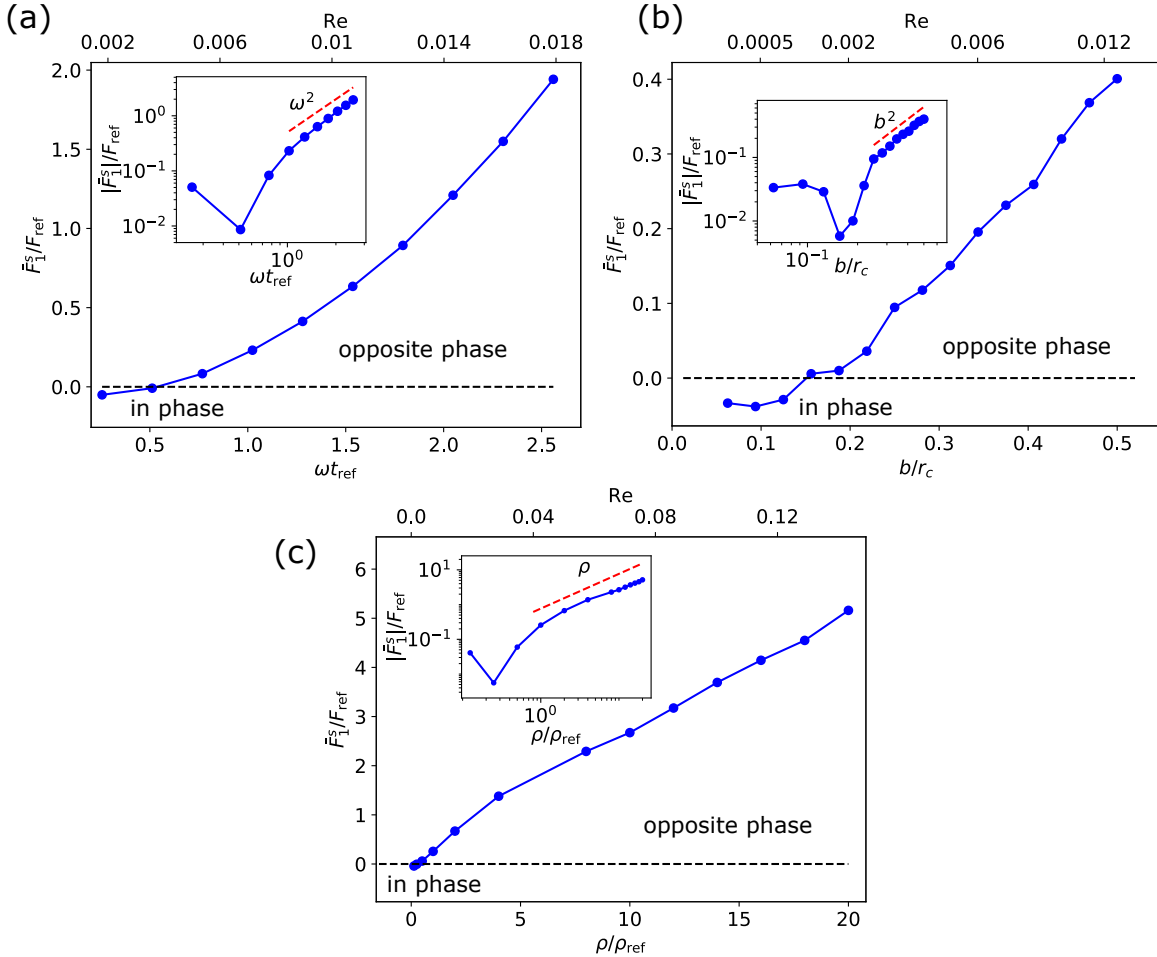


FIG. 4. Synchronization force amplitudes of the first waving sheet (prescribed actuation) for various parameters. (a)  $\bar{F}_1^s$  as a function of wave frequency  $\omega$ .  $b/r_c = 0.375$  and  $\rho/\rho_{\text{ref}} = 1$ . (b)  $\bar{F}_1^s$  as a function of wave amplitude  $b$ .  $\omega t_{\text{ref}} = 1.024$  and  $\rho/\rho_{\text{ref}} = 1$ . (c)  $\bar{F}_1^s$  as a function of fluid mass density  $\rho$ .  $\omega t_{\text{ref}} = 1.024$  and  $b/r_c = 0.375$ . Other parameters, such as  $\eta/\eta_{\text{ref}} = 3.2$ ,  $p_0/p_{\text{ref}} = 2621.4$ , and  $\nu = 7$ , are fixed in all simulations. Insets show absolute values of  $\bar{F}_1^s$  in log scale.

## A. Synchronization in Newtonian fluids

### 1. Interaction of two waving sheets

Figure 3(a) presents synchronization force amplitudes of the first waving sheet with prescribed actuation for different values of  $Re$ , which is controlled by changing the fluid viscosity  $\eta$ . For large enough  $Re$  (or small  $\eta$ ), the synchronization forces favor the opposite-phase configuration, and appear to be independent of  $\eta$ . However, for small  $Re$  values,  $\bar{F}_1^s$  becomes negative, favoring the in-phase configuration. Clearly, the magnitude of  $\bar{F}_1^s$  at small  $Re$  depends on fluid compressibility, which is characterized by the Mach number  $Ma = fb/c$ , where  $c = (p_0\nu/\rho)^{1/2}$  is the speed of sound in SDPD fluid. The importance of fluid compressibility at large values of  $\eta$  can be understood through a slow fluid relaxation by viscous diffusion in response to the prescribed sheet actuation that is independent of  $\eta$ . Figure 3(b) shows that the magnitude of  $\bar{F}_1^s$  at large  $\eta$  is significantly reduced with decreasing  $Ma$ , because local fluid relaxation by sound wave propagation becomes faster for less compressible fluids.

When  $Ma$  is decreased, the transition from opposite-phase to in-phase stable configuration in Fig. 3(a) is shifted toward lower  $Re$  values, and the magnitude of  $\bar{F}_1^s$  in Fig. 3(b) is significantly reduced. Furthermore, in the limit of incompressible fluid at  $Re = 0$ , no synchronization (i.e.  $\bar{F}_1^s = 0$ ) should occur for two interacting sheets having a reflection symmetry with respect to the  $y$  axis [20], which is the case for the imposed sine wave here. These arguments suggest that for an incompressible fluid, inertial effects (i.e.,  $Re > 0$ ) should always lead to the stable opposite-phase configuration with  $\bar{F}_1^s > 0$  that vanishes at  $Re = 0$ . However, if fluid compressibility becomes relevant, the in-phase configuration may occur at low  $Re$ . For comparison, human sperm typically has a beating frequency of  $f \approx 20$  Hz and an amplitude of  $b \approx 10 \mu\text{m}$  [44, 45], resulting in  $Re \approx 2 \times 10^{-3}$  and  $Ma \approx 10^{-7}$  in a water-like environment. For existing microrobots, typical non-dimensional numbers are  $Re \sim 1$  and  $Ma \sim 10^{-5} - 10^{-4}$  [18, 19]. Thus, inertial effects are expected to be pertinent for all microswimmers, while fluid compressibility can be neglected for biological microswimmers such as sperm, but may become relevant for microrobots.

To systematically investigate the synchronization of inextensible sheets, different parameters (other than  $\eta$ ) that affect  $Re$  are varied. Figure 4 shows synchronization force amplitudes of the first waving sheet (prescribed actuation) as a function of wave frequency  $\omega$ , wave amplitude  $b$ , and fluid mass density  $\rho$ . As discussed above, the existence of stable in-phase configuration for all varied parameters is due to fluid-compressibility effects at low  $Re$ . When inertial effects dominate at large enough  $Re$ , the opposite-phase conformation takes place, and the magnitude of  $\bar{F}_1^s$  increases significantly with increasing  $Re$ . Insets in Fig. 4 show that at large enough  $Re$ , the synchronization force amplitude  $\bar{F}_1^s$  exhibits a power-law dependence with respect to the wave frequency  $\omega$ , wave amplitude  $b$ , and fluid mass density  $\rho$ . Remember that  $\bar{F}_1^s$  is independent of fluid viscosity  $\eta$ , when fluid compressibility effects can be neglected, see Fig. 3(a). Therefore, we hypothesize that

$$\bar{F}_1^s \propto \rho \omega^2 b^2 \quad (13)$$

for large enough  $Re$ . Note that Eq. (13) is valid only for small  $bk$ . Figure 5 presents  $\bar{F}_1^s$  as a function of  $bk$  for various  $\omega$ , and shows that for  $bk > 0.4$ , the increase in  $\bar{F}_1^s$  becomes slower than  $b^2$ . As we will show later, an increase in the synchronization force amplitude for large  $bk$  can be much faster than  $b^2$  for viscoelastic fluids.

### 2. Dynamic synchronization of two flexible sheets

To investigate dynamic synchronization process of two beating sheets, we employ the setup with two flexible sheets that have internal actuation. Figure 6(a) shows time-dependent phase difference  $\phi_d$  between two flexible sheets for various fluid viscosities. At low  $\eta$ , the sheets attain the opposite-phase configuration because of inertial effects at large enough  $Re$ . As  $\eta$  is increased, the in-phase configuration becomes stable due to the combined effect of fluid compressibility mentioned above and sheet flexibility that will be discussed below. Note that in the case of internal actuation the wave amplitude  $b$  of flexible sheets is reduced significantly by increasing  $\eta$  [see Fig. 6(b)] because of an increased viscous resistance on the sheets. An increase in viscosity and reduction in the wave amplitude are expected to decrease synchronization forces and increase synchronization time  $\tau^s$  [22]. Nevertheless, the behavior of  $\tau^s$  in Fig. 6(a) is non-monotonic with  $\eta$  due to several reasons. In case of stable opposite-phase configuration ( $\eta/\eta_{\text{ref}} \lesssim 2$  here), where fluid inertial effects dominate,  $\tau^s$  increases with increasing  $\eta$  because the synchronization force amplitude  $\bar{F}^s$  is independent of  $\eta$  [see Fig. 3(a)]. The case of  $\eta/\eta_{\text{ref}} = 3.2$  exhibits the largest  $\tau^s$ , since it is near the opposite-phase to in-phase transition, at which the synchronization force vanishes. With a further increase of viscosity ( $\eta/\eta_{\text{ref}} > 5$ ) for the in-phase configuration, although the magnitude of  $\bar{F}^s$  increases, frictional forces on the sheets lead to larger  $\tau^s$  values for larger  $\eta$ .

To directly demonstrate the effect of sheet flexibility, Fig. 7(a) presents the transition from opposite-phase to in-phase configuration when sheet flexibility is increased by decreasing the spring stiffness  $\zeta_s$ . Here, fluid compressibility



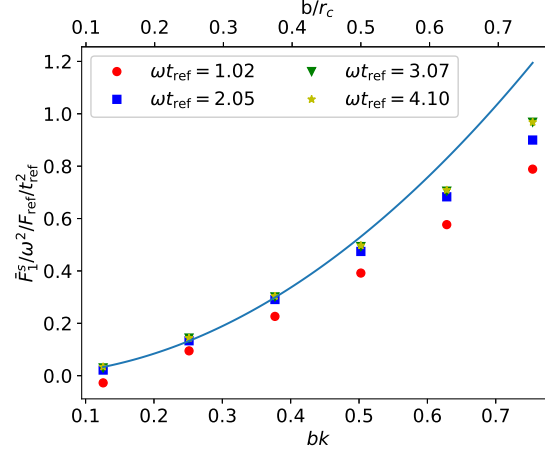


FIG. 5. Synchronization force amplitudes with non-negligible inertia as a function of  $bk$ . The solid line represents a fit with quadratic function. Note that for  $bk > 0.4$ , the relation  $\bar{F}_1^s \propto b^2$  no longer holds. Here,  $\eta/\eta_{\text{ref}} = 3.2$ ,  $\rho/\rho_{\text{ref}} = 1$ ,  $p_0/p_{\text{ref}} = 2621.4$ , and  $\nu = 7$ .

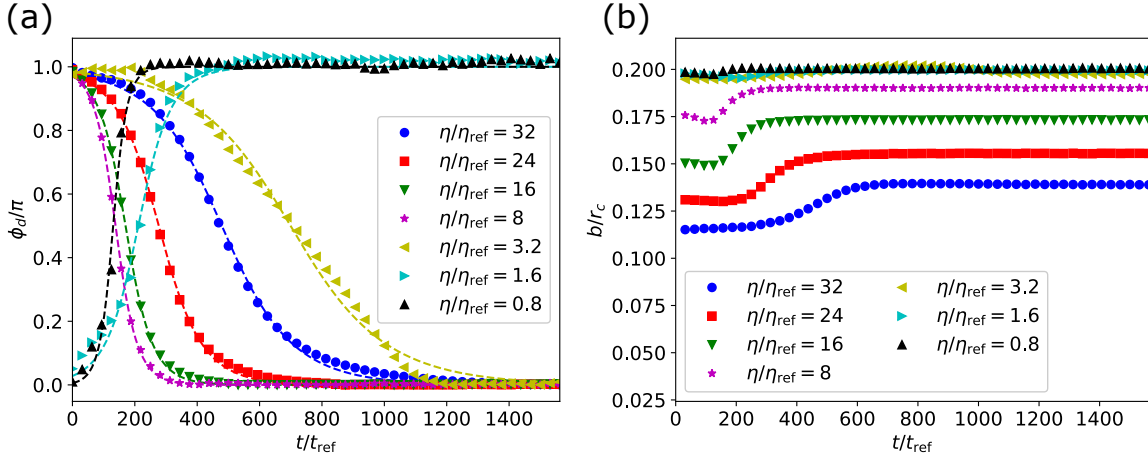


FIG. 6. Dynamic synchronization of two flexible sheets (internal actuation) for different fluid viscosities. (a) Phase difference plotted by symbols as a function of time. The dashed lines correspond to data fitting using Eq. (15). (b) Beating wave amplitude  $b$  for various  $\eta$ . Here,  $\omega t_{\text{ref}} = 2.56$ ,  $\theta_b/\pi = 0.028$ ,  $\zeta_s/\zeta_{\text{ref}} = 4096$  ( $\kappa/\kappa_{\text{ref}} = 288$ ),  $\rho/\rho_{\text{ref}} = 1$ ,  $p_0/p_{\text{ref}} = 40.96$ , and  $\nu = 5$ .

effects can be neglected due to a low fluid viscosity of  $\eta/\eta_{\text{ref}} = 3.2$ . Interestingly, stiff sheets (i.e., large  $\zeta_s$  and  $\kappa$ ) synchronize toward the opposite-phase configuration due to inertial effects, while soft sheets are driven toward the in-phase conformation, even though the effective  $\text{Re}$  increases with decreasing  $\kappa$  due to an increase in wave amplitude, see Fig. 7(b). Therefore, sheet flexibility drives the system of two sheets toward the in-phase configuration. This result is consistent with the theory predicting that a finite elasticity of two sheets in an incompressible fluid is sufficient to break the symmetry and exhibit the in-phase synchronization at  $\text{Re} = 0$  [26]. Furthermore, a simulation study [23] of a pair of flexible sheets based on the incompressible Navier-Stokes equations reports the transition from in-phase to opposite-phase conformation with increasing  $\text{Re}$ , in agreement with the discussed results.

Our simulations demonstrate that the synchronization forces  $F_1^s$  and  $F_2^s$  have a sine-function dependence on  $\phi_d$  [see Eq. (12)], independently of the contributing factors, such as fluid compressibility, inertial effects, and sheet flexibility. Therefore, the dynamic synchronization process can be described as a damped harmonic oscillator

$$\frac{d^2 \phi_d}{dt^2} = -a_1 \frac{d\phi_d}{dt} - a_2 \sin(\phi_d), \quad (14)$$

where  $a_1$  is a damping coefficient and  $a_2$  corresponds to the synchronization force amplitudes  $\bar{F}_1^s$  and  $\bar{F}_2^s$ , which are either negative or positive, depending on whether the in-phase or opposite-phase configuration is stable. In general,

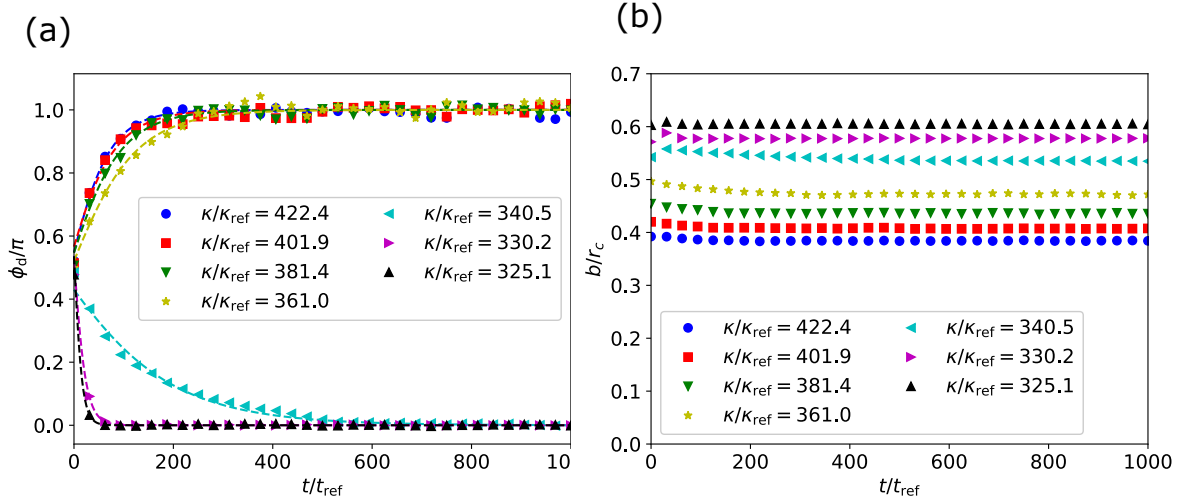


FIG. 7. Synchronization of two flexible sheets for various flexural rigidities  $\kappa$ . (a) Phase difference  $\phi_d$ . Simulated data are shown by symbols, while the dashed lines represent fits using Eq. (15). (b) Wave amplitude  $b$ . Here,  $\zeta_s/\zeta_{\text{ref}} \in [41, 819.2]$ ,  $\omega t_{\text{ref}} = 2.048$ ,  $\eta/\eta_{\text{ref}} = 3.2$ ,  $\rho/\rho_{\text{ref}} = 1$ ,  $\theta_b/\pi = 0.044$ ,  $p_0/p_{\text{ref}} = 2621.4$ , and  $\nu = 7$ .

$a_1$  can be a function of  $\phi_d$ , but for simplicity, it is assumed to be constant here. A process described by Eq. (14) can have an oscillating dynamics, if the inertial term represented by the second time derivative is large enough. Our simulations (not presented here) have shown that an oscillation in the synchronization of two flexible sheets may occur at low fluid viscosities  $\eta/\eta_{\text{ref}} < 0.08$ . As the employed viscosity values  $\eta/\eta_{\text{ref}} \gg 0.08$ , the synchronization process of two sheets can be considered overdamped, even though it is often caused by inertial effects. By neglecting the inertial term in Eq. (14), an Adler-like equation [46]  $d\phi_d/dt = -a_2/a_1 \sin(\phi_d)$  for  $\phi_d$  is obtained, which has an analytical solution given by [47]

$$\phi_d = 2 \tan^{-1} \left( \tan \frac{\phi_d^0}{2} e^{-a_2 t/a_1} \right), \quad (15)$$

where  $\phi_d^0$  is the initial phase difference at time  $t = 0$ . Equation (15) is used to fit the simulation data in Figs. 6(a) and 7(a), where the fits are shown by dashed lines. Clearly, the fits are very good, and allow the extraction of synchronization time  $\tau^s = |a_1/a_2|$  from the simulation data of time-dependent synchronization.

Let us consider  $a_1 \propto \eta$ , since it represents damping effects, and  $a_2 = \bar{F}_1^s \propto \rho \omega^2 b^2$  [see Eq. (13)], which has been hypothesized for two waving sheets at high enough Re. Then, the synchronization time  $\tau^s$  normalized by the wave frequency  $\omega$  simply becomes

$$\tau^s \omega \propto \frac{1}{\text{Re}}. \quad (16)$$

This relation is tested by a number of simulations for various  $\omega$ ,  $\rho$ ,  $\eta$ , and  $\theta_b$  values. Figure 8(a) shows  $\tau^s$  for the flexural rigidity  $\kappa/\kappa_{\text{ref}} = 221.2$  and EoS parameter  $p_0/p_{\text{ref}} = 2621.4$  as a function of Re. When inertial effects dominate at large enough Re,  $\tau^s$  is inversely proportional to Re, as predicted. At low Re values, the effects of fluid compressibility and sheet flexibility become important, so that  $\tau^s$  deviates from this relation. Figure 8(b) presents simulation data for  $\kappa/\kappa_{\text{ref}} = 364.8$  and  $p_0/p_{\text{ref}} = 10485.6$ , such that both fluid compressibility and sheet flexibility effects are significantly reduced. The behavior of  $\tau^s$  closely follows the relation in Eq. (16) for a wide range of Re numbers. Noteworthy, the rapid increase in  $\tau^s$  at small Re in Fig. 8 is qualitatively consistent with the theoretical prediction that no synchronization of two inextensible sheets having a reflection symmetry with respect to the  $y$  axis can occur at  $\text{Re} = 0$  [43].

## B. Synchronization in viscoelastic fluids

Fluid elasticity is also sufficient to break the symmetry and result in the in-phase synchronization of two inextensible sheets at  $\text{Re} = 0$  [27]. Theoretical prediction for the synchronization force between two sheets up to the order  $\mathcal{O}(b^2 k^2)$

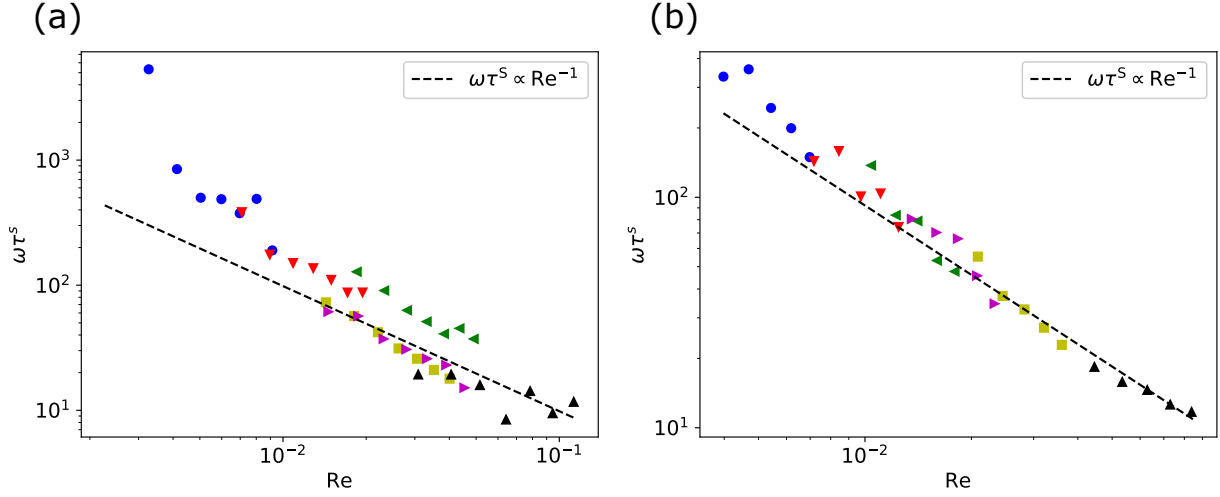


FIG. 8. Dependence of synchronization time  $\tau^s$  on  $\omega$  and  $\text{Re}$ . (a) Simulations with flexural rigidity  $\kappa/\kappa_{\text{ref}} = 221.2$  and the EoS parameter  $p_0/\rho_{\text{ref}} = 2621.4$ . Different data sets are plotted by symbols, corresponding to  $\eta/\eta_{\text{ref}} = 3.2$ ,  $\rho/\rho_{\text{ref}} = 1$ , and  $\theta_b/\pi = 0.028$  (blue circles);  $\eta/\eta_{\text{ref}} = 3.2$ ,  $\rho/\rho_{\text{ref}} = 1$ , and  $\theta_b/\pi = 0.044$  (red down-pointing triangles);  $\eta/\eta_{\text{ref}} = 3.2$ ,  $\rho/\rho_{\text{ref}} = 1$ , and  $\theta_b/\pi = 0.089$  (green left-pointing triangles);  $\eta/\eta_{\text{ref}} = 1.6$ ,  $\rho/\rho_{\text{ref}} = 1$ , and  $\theta_b/\pi = 0.044$  (yellow squares);  $\eta/\eta_{\text{ref}} = 3.2$ ,  $\rho/\rho_{\text{ref}} = 2$ , and  $\theta_b/\pi = 0.044$  (purple right-pointing triangles);  $\eta/\eta_{\text{ref}} = 3.2$ ,  $\rho/\rho_{\text{ref}} = 4$ , and  $\theta_b/\pi = 0.044$  (black up-pointing triangles). (b) Simulations with  $\kappa/\kappa_{\text{ref}} = 364.8$  and  $p_0/\rho_{\text{ref}} = 10485.6$ . Various symbols represent  $\eta/\eta_{\text{ref}} = 3.2$ ,  $\rho/\rho_{\text{ref}} = 1$ , and  $\theta_b/\pi = 0.044$  (blue circles);  $\eta/\eta_{\text{ref}} = 3.2$ ,  $\rho/\rho_{\text{ref}} = 1$ , and  $\theta_b/\pi = 0.067$  (red down-pointing triangles);  $\eta/\eta_{\text{ref}} = 3.2$ ,  $\rho/\rho_{\text{ref}} = 1$ , and  $\theta_b/\pi = 0.089$  (green left-pointing triangles);  $\eta/\eta_{\text{ref}} = 1.6$ ,  $\rho/\rho_{\text{ref}} = 1$ , and  $\theta_b/\pi = 0.089$  (yellow squares);  $\eta/\eta_{\text{ref}} = 3.2$ ,  $\rho/\rho_{\text{ref}} = 1$ , and  $\theta_b/\pi = 0.11$  (purple right-pointing triangles);  $\eta/\eta_{\text{ref}} = 3.2$ ,  $\rho/\rho_{\text{ref}} = 4$ , and  $\theta_b/\pi = 0.089$  (black up-pointing triangles). Each set of data includes several  $\omega t_{\text{ref}}$  values in the range  $[1.02, 2.56]$  and  $\nu = 7$  in all simulations. The dashed lines indicate  $\text{Re}^{-1}$ .

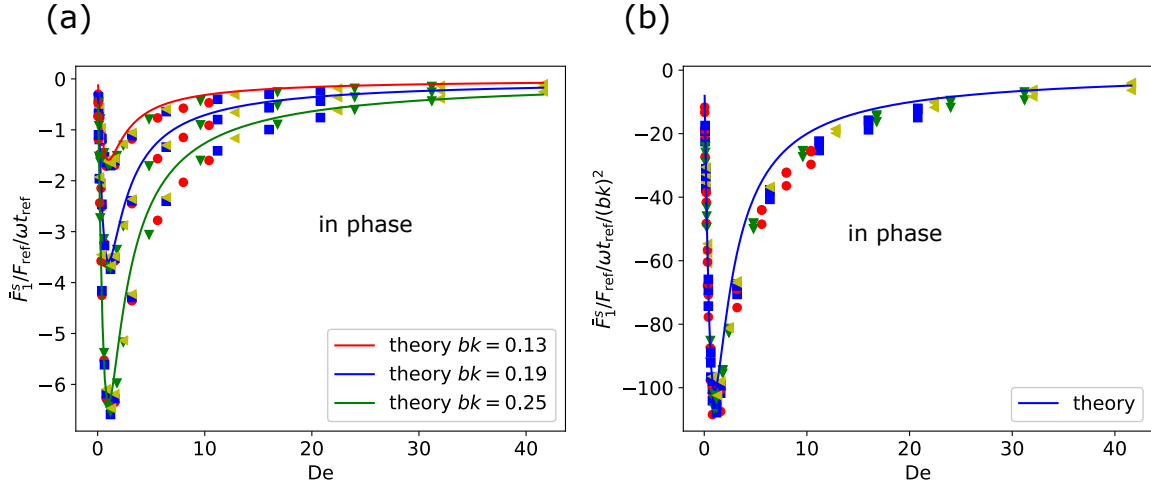


FIG. 9. Synchronization force amplitudes of two waving sheets (prescribed actuation) in viscoelastic fluids. (a)  $\bar{F}_1^s/\omega$  and (b)  $\bar{F}_1^s/\omega/(bk)^2$  as a function of  $\text{De}$  for various  $bk$ . Different simulation data sets are plotted by symbols, corresponding to  $\omega t_{\text{ref}} = 1.024$  (red circles);  $\omega t_{\text{ref}} = 2.048$  (blue squares);  $\omega t_{\text{ref}} = 3.072$  (green down-pointing triangles);  $\omega t_{\text{ref}} = 4.096$  (yellow left-pointing triangles). Solid lines are theoretical predictions [27] from Eq. (17). Here,  $\eta_s/\eta_{\text{ref}} = 3.0$ ,  $\eta_p/\eta_{\text{ref}} = 13.0$ , and  $\rho/\rho_{\text{ref}} = 1$ .

is given by [27]

$$\frac{F_1^s(\phi_d)k}{\omega\eta} = \left[ \frac{2\pi\Delta U}{kh} - \frac{4\pi\text{De}\eta_p}{\eta(1+\text{De}^2)} A(kh) \sin(\phi_d) \right] (bk)^2, \quad A(kh) = \frac{kh \cosh(kh) + \sinh(kh)}{\cosh(2kh) - 2k^2h^2 - 1}, \quad (17)$$

where  $\Delta U$  is the relative velocity of two sheets and  $\eta = \eta_p + \eta_s$  includes polymer and solvent viscosity contributions. In case of two waving sheets with prescribed actuation,  $\Delta U = 0$ . Note that for  $\Delta U = 0$ , the synchronization force in

Eq. (17) can be written as  $F_1^s(\phi_d) = \bar{F}_1^s \sin(\phi_d)$ , which is identical to Eq. (12) hypothesized before.

Figure 9(a) presents the ratio  $\bar{F}_1^s/\omega$  obtained from a number of simulations (symbols) of two waving sheets in viscoelastic fluids with respect to the theoretical prediction (solid lines) in Eq. (17) for several  $bk$  values. An excellent agreement between simulated and theoretical synchronization force amplitudes is achieved. In these simulations, the wave frequency  $\omega t_{\text{ref}} \in [1.024, 4.096]$ , wave amplitude  $b/r_c \in [0.125, 0.25]$ , and the relaxation time  $\tau/t_{\text{ref}} \in [0.04, 10.16]$  are varied, while the viscosities  $\eta_s/\eta_{\text{ref}} = 3.0$  and  $\eta_p/\eta_{\text{ref}} = 13.0$  are kept constant. Note that the value of  $N_p$  is adjusted according to changes in  $\tau$  in order to keep  $\eta_p = k_B T d_0 N_p \tau$  fixed. Furthermore, mass density of the fluid is set to be relatively small  $\rho/\rho_{\text{ref}} = 0.0625$  to minimize inertial effects, and the EoS parameters ( $p_0/p_{\text{ref}} = 6553.6$  and  $\nu = 7$ ) are chosen such that fluid compressibility effects can be neglected.

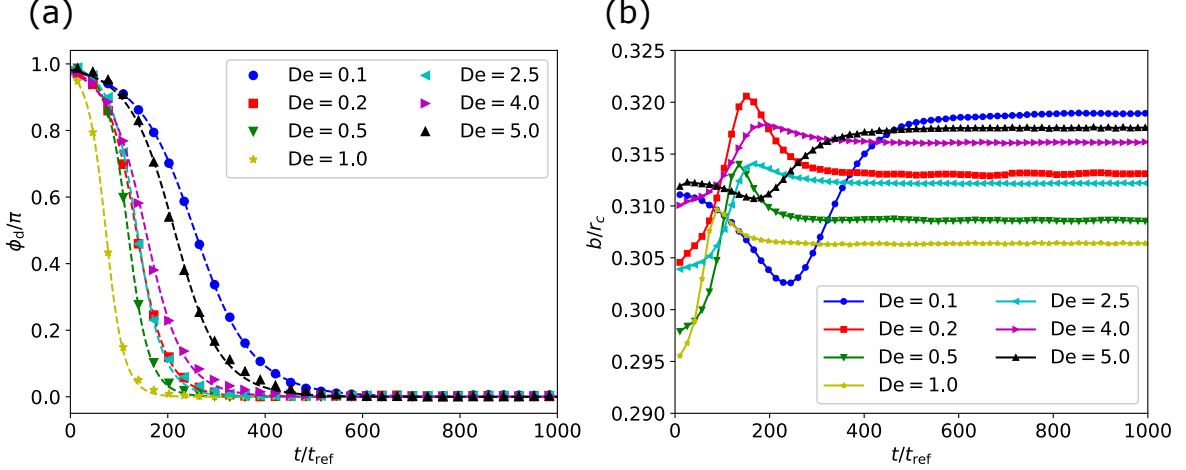


FIG. 10. Dynamic synchronization of two flexible sheets mediated by fluid viscoelasticity. (a) Phase difference  $\phi_d$  as a function of time for different De. Dashed lines represent fits using Eq. (15). (b) Beating wave amplitudes. Here,  $\eta_s/\eta_{\text{ref}} = 3.0$ ,  $\eta_p/\eta_{\text{ref}} = 13.0$ ,  $\omega t_{\text{ref}} = 1.28$ ,  $\rho/\rho_{\text{ref}} = 0.125$ ,  $\theta_b/\pi = 0.056$ ,  $\zeta_s/\zeta_{\text{ref}} = 4096$  ( $\kappa/\kappa_{\text{ref}} = 288$ ),  $p_0/p_{\text{ref}} = 6553.6$ , and  $\nu = 7$ .

Figure 9(b) demonstrates that the simulated force amplitudes scaled as  $\bar{F}_1^s/\omega/(bk)^2$  fall onto a single master curve that is well captured by the theoretical prediction in Eq. (17). Furthermore, Fig. 9 shows that the maximum synchronization force is achieved at  $De = 1$  for a fixed  $bk$  and  $\omega$ . Noteworthy, for a fixed  $\omega$ , the synchronization force amplitude asymptotically approaches zero with increasing De or  $\tau$ . This indicates that the synchronization of flagellated microswimmers must be weak in viscoelastic fluids with a large relaxation time. In fact, De for realistic biological microswimmers can be significantly larger than unity. For instance, De is between  $10^2$  and  $10^3$  for the case of sperm cells swimming in mucus, whose relaxation time is in the range of  $1 \sim 10$  s [27].

Figure 10(a) presents dynamic synchronization of two flexible sheets for various De, and demonstrates that this process is fastest at  $De = 1$ , in agreement with the theoretical prediction in Eq. (17). The corresponding beating wave amplitudes shown in Fig. 10(b) are small enough in these simulations, such that the theoretical prediction is accurate. Interestingly, the synchronization times in viscoelastic fluids have similar magnitudes as those in Newtonian fluids (compare with Figs. 6 and 7).

According to the theoretical prediction in Eq. (17) [27], the synchronization forces resulting from fluid viscoelasticity are of the order  $\mathcal{O}(b^2k^2)$ , which is similar to the synchronization forces originating from inertial effects, see Eq. (13). Therefore, it is plausible to expect the transition from in-phase to opposite-phase configuration with increasing Re in viscoelastic fluids. Figure 11 illustrates the competing effects of viscoelasticity and inertia, and demonstrates the existence of in-phase to opposite-phase transition at high enough Re by increasing  $\rho$ . For negligible inertial effects ( $\rho/\rho_{\text{ref}} = 0.0625$ ),  $\bar{F}_1^s$  exhibits a plateau at large De, consistently with the theoretical prediction in Eq. (17). As  $\rho$  is increased, inertial effects become more prominent, and the opposite-phase configuration might be attained. For comparison, when  $\omega t_{\text{ref}} = 4.096$  ( $De = 16$ ),  $\rho/\rho_{\text{ref}} = 0.0625$  leads to  $Re = 1.6 \times 10^{-4}$ , while  $\rho/\rho_{\text{ref}} = 1$  corresponds to  $Re = 2.5 \times 10^{-3}$ .

The prediction that synchronization of two sheets with a fixed  $\omega$  is weak at large De seemingly disagrees with recent experimental [29] and numerical [48] studies on sperm interaction, which demonstrate that fluid viscoelasticity can significantly enhance clustering. Note that the theoretical prediction by Taylor [12] in Eq. (10) is of the order  $\mathcal{O}(b^4k^4)$ , and has been shown to be accurate for  $bk \lesssim 0.4$  [49]. The theoretical prediction in Eq. (17) for Oldroyd-B fluids [27] is of the order  $\mathcal{O}(b^2k^2)$ , such that it is reliable for small  $bk$  as verified by our simulations in Fig. 9, but is expected to be less accurate for large  $bk$  values. Furthermore, there exist a number of experimental studies [5, 7, 29, 45] with flagellated microswimmers, whose wave amplitude is large enough to make the assumption of small  $bk$  invalid. Figure

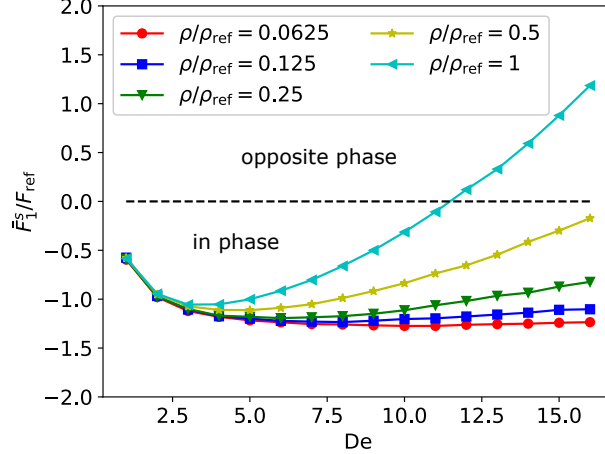


FIG. 11. Synchronization force amplitudes of two waving sheets in viscoelastic fluids for different fluid densities, affecting the value of  $Re$ .  $De$  is varied by changing  $\omega t_{ref} \in [0.256, 4.096]$ . For instance, when  $\omega t_{ref} = 4.096$  ( $De = 16$ ),  $Re = 1.6 \times 10^{-4}$  for  $\rho/\rho_{ref} = 0.0625$  and  $Re = 2.5 \times 10^{-3}$  for  $\rho/\rho_{ref} = 1$ . Other parameters  $b/r_c = 0.25$ ,  $\eta_s/\eta_{ref} = 6.0$ ,  $\eta_p/\eta_{ref} = 10$ ,  $\tau/t_{ref} = 3.9$ ,  $p_0/p_{ref} = 6553.6$ , and  $\nu = 7$  remain fixed.

12 shows synchronization force amplitudes of two waving sheets in viscoelastic fluids for  $bk = 0.5$ ,  $bk = 0.63$ , and  $bk = 0.75$ . The simulation parameters here are the same as those in Fig. 9. Clearly, the simulated  $\bar{F}_1^s$  values for large  $bk$  are significantly larger than those predicted theoretically at large  $De$ . This demonstrates that for  $bk > 0.4$ , fluid viscoelasticity plays a much more prominent role for sheet synchronization than predicted theoretically for small  $bk$ . Interestingly, the dependence of  $\bar{F}_1^s$  on  $bk > 0.4$  has an exponent that can be significantly larger than two. For comparison, an increase in the synchronization force for Newtonian fluids at large enough  $Re$  and  $bk > 0.4$  is slower than  $b^2$ , as shown in Fig. 5. Therefore, our simulations demonstrate that fluid viscoelasticity is the main cause of a tremendous increase in synchronization forces at large  $bk$  and  $De$ , providing a plausible explanation for the enhanced clustering of flagellated microswimmers in viscoelastic fluids.

Note that the Oldroyd-B model becomes unphysical when the Weissenberg number, which relates fluid relaxation time to the time determined by a characteristic strain rate, approaches  $Wi \approx 1$ . As a precautionary step, the Oldroyd-B model has been tested using Kolmogorov flow, leading to accurate results for  $Wi \lesssim 0.8$ , while for  $Wi \gtrsim 0.9$  the SDPD simulations become unstable. For the synchronization problem of two sheets, Weissenberg number can be defined as  $Wi = bk\omega\tau/(2\pi)^2$ . For example, simulation results in Fig. 9 agree well with the analytical solution in Eq. (17) and correspond to  $Wi \in [2.5 \times 10^{-4}, 0.26]$  for  $bk = 0.25$ . For comparison,  $Wi \in [5 \times 10^{-4}, 0.41]$  for  $bk = 0.5$  in Fig. 12(a),  $Wi \in [6.4 \times 10^{-4}, 0.36]$  for  $bk = 0.63$  in Fig. 12(b), and  $Wi \in [7.6 \times 10^{-4}, 0.24]$  for  $bk = 0.75$  in Fig. 12(c). Therefore, all presented results are well within the limit of Oldroyd-B model applicability, confirming that the dramatic increase in synchronization forces at large  $De$  and  $bk$  is not due to any model shortcomings.

### C. Swimming efficiency of two synchronized sheets

Different mechanisms, such as inertia, sheet elasticity, and fluid compressibility and viscoelasticity, can contribute to the synchronization of two sheets. An interesting question is whether the behavior of two synchronized sheets is different from that of a single sheet. In the early work of Taylor [12], it has been shown that energy dissipation of two sheets at  $Re = 0$  is minimized (maximized) when they attain the in-phase (opposite-phase) configuration. More recent theoretical study [20] reports that the stable synchronized phase is not necessarily the phase with a minimum energy dissipation. There exist numerous examples of biological micro-organisms swimming in clusters, suggesting that collective swimming may have some advantages. A numerical study about sperm swimming [6] reports that clustered sperms swim slower, and consume a lower amount of energy per sperm than a single one alone. However, it is not clear whether different factors (e.g., inertia, sheet elasticity, and fluid viscoelasticity) affect the properties of synchronized sheets in a qualitatively similar way.

Figure 13 compares output power, swimming velocity and efficiency of a pair of synchronized sheets with those of a single sheet. In these simulations, two sheets are let to fully synchronize, and after that the aforementioned measurements are performed. Three different synchronization factors are considered, including sheet synchronization domi-

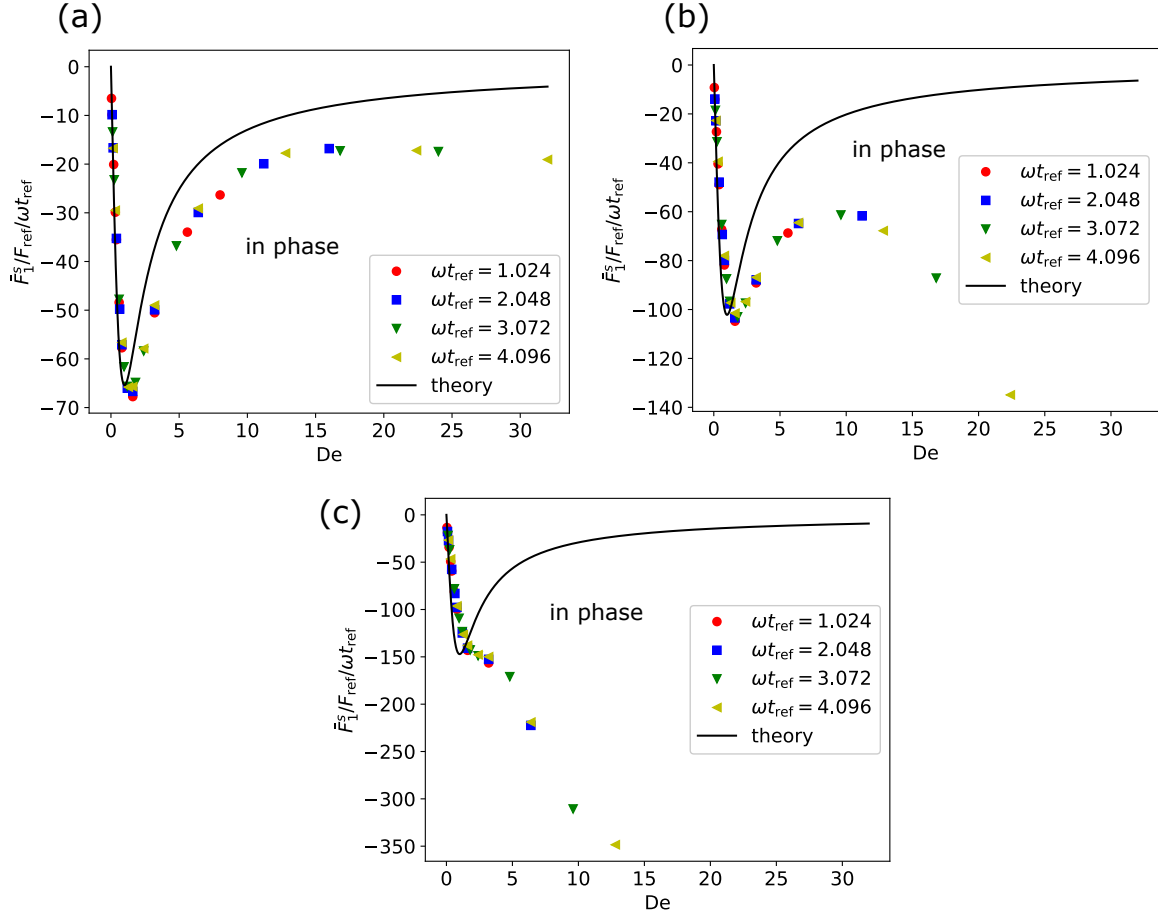


FIG. 12. Synchronization force amplitudes as a function of  $De$  for (a)  $bk = 0.5$ , (b)  $bk = 0.63$ , and (c)  $bk = 0.75$ . As  $bk$  is increased, synchronization forces strongly increase at large enough  $De$ . Note that for large  $bk$ , the dependence of  $F_1^s$  on phase difference  $\phi_d$  is no longer a sine function. Therefore,  $F_1^s$  corresponds to the maximum of  $F_1^s(\phi_d)$  here. Other parameters  $\eta_s/\eta_{ref} = 3.0$ ,  $\eta_p/\eta_{ref} = 13.0$ ,  $\rho/\rho_{ref} = 0.0625$ ,  $p_0/p_{ref} = 6553.6$ , and  $\nu = 7$  remain fixed.

nated by inertial effects (denoted as “IN”), sheet elasticity (abbreviated as “SE”), and fluid viscoelasticity (denoted by “VE”). Figure 13(a) presents total output power for the three cases, which is computed as  $P = -\sum_{i \leq N} \sum_{j \leq M} \mathbf{F}_{ij} \cdot \mathbf{v}_i$ , where  $N$  is the total number of sheet particles,  $M$  is the total number of fluid particles, and  $\mathbf{F}_{ij}$  are inter-particle forces. Note that only for the inertia-dominated case, the output power of a synchronized pair is larger than that of a single sheet. This is due to the fact that the sheets synchronize to the opposite-phase conformation, for which the dissipation energy is largest in Stokes flow regime ( $Re$  here is smaller than 0.04). Interestingly, swimming velocities of a synchronized pair and a single sheet do not differ much, see Fig. 13(b). Only in the “SE” case, the swimming velocity of a single sheet is slightly larger than that of the pair. These results indicate that only in the “VE” case, the synchronized pair of sheets swims not slower than the corresponding single sheet, and has a lower output power.

Figure 13(c) presents swimming efficiency  $\mathcal{E} = (P - P_{eff})/P$  for different cases, where  $P_{eff} = F_x^{visc} V_x$  is the effective power with  $F_x^{visc}$  being the  $x$  component of viscous forces exerted by the fluid on the sheets and  $V_x$  is the swimming speed. In the case of dominating inertial effects, the swimming efficiency (about 2–3%) is largest, and the synchronized pair is slightly more efficient than a single sheet. In the case when sheet-elasticity effects dominate, the pair has a lower efficiency than the single sheet. Finally, in case of dominating viscoelastic contributions, the swimming efficiency is smallest and there is no difference in  $\mathcal{E}$  for the synchronized pair and single sheet. Nevertheless, swimming efficiency may not be an appropriate measure to clearly determine possible advantages/disadvantages of synchronized swimming. For example, for the “IN” case in Fig. 13, the efficiency and total output power are larger for the synchronized pair than for the single sheet, but the swimming speed is nearly the same. In this case, the sheets synchronize toward the opposite-phase configuration, which results in a relatively strong backward (peristaltic-like) flow between them, thus increasing the resistance for swimming. Finally, Fig. 13(d) shows that wave amplitudes are nearly the same for both the synchronized pair and single sheet in all cases.

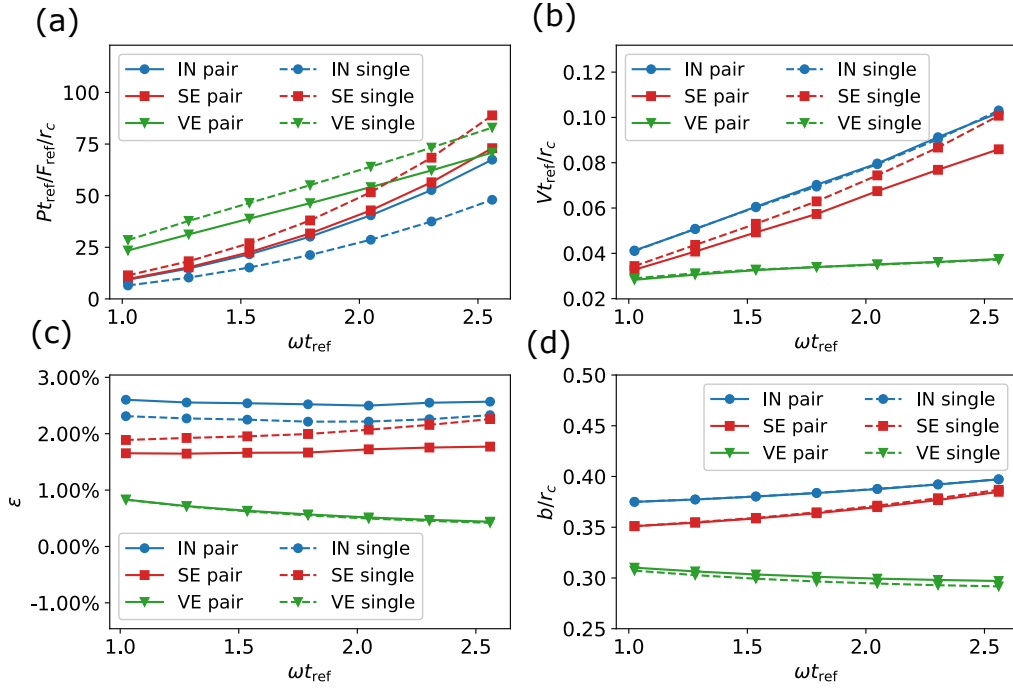


FIG. 13. Swimming properties of two synchronized sheets in comparison to a single sheet. (a) Sheet output power  $P$ , (b) swimming velocity  $V$ , (c) swimming efficiency  $\mathcal{E}$ , and (d) beating amplitude  $b$  for various conditions. The abbreviation “IN” denotes Newtonian-fluid simulations, in which inertial effects dominate, with the following parameters  $\eta/\eta_{\text{ref}} = 1.6$ ,  $\rho/\rho_{\text{ref}} = 1$ ,  $\theta_b/\pi = 0.044$ ,  $\zeta_s/\zeta_{\text{ref}} = 1638.4$  ( $\kappa/\kappa_{\text{ref}} = 211.2$ ),  $p_0/p_{\text{ref}} = 2621.4$ , and  $\nu = 7$ . The abbreviation “SE” denotes Newtonian-fluid simulations, in which the effect of sheet flexibility dominates, with simulation parameters  $\eta/\eta_{\text{ref}} = 3.2$ ,  $\rho/\rho_{\text{ref}} = 1$ ,  $\theta_b/\pi = 0.028$ ,  $\zeta_s/\zeta_{\text{ref}} = 81.92$  ( $\kappa/\kappa_{\text{ref}} = 162.6$ ),  $p_0/p_{\text{ref}} = 819.2$ , and  $\nu = 7$ . “VE” corresponds to non-Newtonian-fluid simulations with dominating viscoelastic effects for simulation parameters  $\eta_s/\eta_{\text{ref}} = 3.0$ ,  $\eta_p/\eta_{\text{ref}} = 13.0$ ,  $\tau/t_{\text{ref}} = 2.0$ ,  $\rho/\rho_{\text{ref}} = 0.125$ ,  $\theta_b/\pi = 0.056$ ,  $\zeta_s/\zeta_{\text{ref}} = 4096$  ( $\kappa/\kappa_{\text{ref}} = 288$ ),  $p_0/p_{\text{ref}} = 6553.6$ , and  $\nu = 7$ .

TABLE II. Different factors which lead to the synchronization of two sheets toward the in-phase or opposite-phase configurations. When several factors are present, the final configuration is determined by their competition.

| Factors                        | Theory  | Simulation  |
|--------------------------------|---|---|
| No inertia ( $\text{Re} = 0$ ) | No synchronization (incompressible fluid, inextensible sheets) [20]                               |   |
| Inertia ( $\text{Re} > 0$ )    |   | Opposite-phase configuration (this study and Ref. [23]) |
| Asymmetric wave                | In-phase or opposite-phase configuration, depending on the asymmetry ( $\text{Re} = 0$ ) [20, 22] |   |
| Sheet flexibility              | In-phase configuration ( $\text{Re} = 0$ ) [26]   | In-phase configuration ( $\text{Re} > 0$ , this study)  |
| Fluid compressibility          |   | In-phase configuration ( $\text{Re} > 0$ , this study)  |
| Fluid viscoelasticity          | In-phase configuration [27]   | In-phase configuration (this study and Ref. [28])       |

#### IV. CONCLUSIONS

We have employed numerical simulations to study the effect of inertia, sheet flexibility, and fluid compressibility and viscoelasticity on the synchronization of two inextensible or flexible sheets. Table II shows the summary of all results. Inertial effects always lead to sheet synchronization toward the opposite-phase configuration. When inertial effects dominate, the synchronization time  $\tau^s$  of two sheets is inversely proportional to the Reynolds number, such that  $\tau^s \omega \propto \text{Re}^{-1}$ . Both fluid compressibility and sheet flexibility drive synchronization toward the in-phase configuration, and compete with inertial effects for  $\text{Re} > 0$ . Furthermore, we have systematically tested the theoretical prediction [27] of the synchronization forces between two sheets in viscoelastic fluids, favoring the in-phase configuration. Our simulation results are in excellent agreement with the theoretical prediction for  $bk < 0.4$ ; however, for large  $bk$ ,

synchronization forces strongly depart from the theory for  $De > 1$ , indicating a rapid synchronization. Thus, for  $De > 1$  and large enough  $bk$ , fluid viscoelasticity has a dramatic effect on the synchronization of two sheets, which clearly dominates over other factors, such as inertia and sheet elasticity. This result is consistent with the observations of significant enhancement of sperm clustering in viscoelastic fluids [29]. Finally, sheet synchronization dominated by fluid viscoelasticity does not impede swimming velocity of the synchronized pair, but has a lower output power in comparison to a single sheet.

Simulation results presented here constitute a systematic study of competing effects for the synchronization of two sheets. They can be used to qualitatively assess the importance of possible factors for experimentally-observed interactions between biological microswimmers or artificial microrobots. This knowledge is useful for a better understanding of collective behavior of microswimmers and for tuning of synchronization interactions between artificial microrobots.

### ACKNOWLEDGMENTS

C.M. acknowledges funding by the China Scholarship Council (CSC) and German Academic Exchange Service (DAAD) through the Sino-German (CSC-DAAD) Postdoc Scholarship Program. We gratefully acknowledge the computing time granted through JARA-HPC on the supercomputer JURECA [50] at Forschungszentrum Jülich.

### Appendix A: Calculation of flexural rigidity $\kappa$

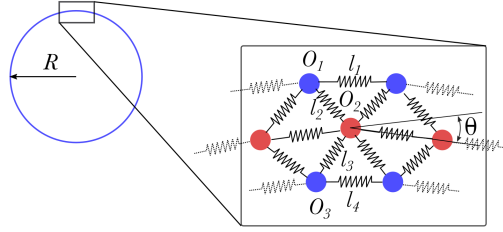


FIG. 14. Schematic of a ring used for the calculation of sheet flexural rigidity  $\kappa$ .  $R$  is the ring radius,  $l_1, \dots, l_4$  are lengths of the corresponding springs, and  $\theta$  is the angle between two adjacent springs in the middle layer. Equilibrium lengths are  $l_1^0 = l_4^0 = l_0$  and  $l_2^0 = l_3^0 = \sqrt{5}l_0/2$ .

We consider a ring (see Fig. 14) whose structure is similar to the sheet in Fig. 1(b). In continuum, elastic energy of the ring is given by

$$E = \frac{\kappa}{2} \int_{2\pi R} \frac{dl}{R^2} = \frac{\pi\kappa}{R}, \quad (\text{A1})$$

which can be compared with the energy of a discrete structure. The force balance at  $O_1$  yields

$$2\zeta_s(l_1 - l_0) \sin \frac{\theta}{2} = 2\zeta_s \left( \frac{\sqrt{5}}{2}l_0 - l_2 \right) \cdot \frac{2}{\sqrt{5}}, \quad (\text{A2})$$

resulting in

$$l_2 \approx \frac{\sqrt{5}}{2}(l_0 - \Delta l \frac{\theta}{2}), \quad (\text{A3})$$

with  $\Delta l = l_1 - l_0$ . Under the assumption that the middle layer does not deform, the force balance at  $O_2$  leads to  $l_2 = l_3$ . From the discrete geometry in Fig. 14, we obtain

$$\frac{R}{l_0} = \frac{R + \frac{2}{\sqrt{5}}l_2}{l_0 + \Delta l} \Rightarrow \Delta l = \frac{2l_0^2 R}{2R^2 + l_0^2}. \quad (\text{A4})$$

Then, the elastic energy of the discrete structure is given by

$$E_d = N\zeta_s(\Delta l^2 + \frac{5}{8}\Delta l^2\theta^2) + N\frac{\zeta_s}{2}\theta^2. \quad (\text{A5})$$



By substituting  $\Delta l$  and  $\theta = l_0/R$  into the equation above, we obtain

$$E_d \approx \frac{2\pi\zeta_s l_0^3 + \pi\zeta_\theta l_0}{R}, \quad (\text{A6})$$

which results, when compared with Eq. (A1), in the expression for flexural rigidity  $\kappa$  as

$$\kappa = 2\zeta_s l_0^3 + \zeta_\theta l_0. \quad (\text{A7})$$

- 
- [1] E. Lauga and T. R. Powers, “The hydrodynamics of swimming microorganisms,” *Rep. Prog. Phys.* **72**, 096601 (2009).
- [2] J. Elgeti, R. G. Winkler, and G. Gompper, “Physics of microswimmers - single particle motion and collective behavior: a review,” *Rep. Prog. Phys.* **78**, 056601 (2015).
- [3] C. Bechinger, R. Di Leonardo, H. Löwen, C. Reichhardt, G. Volpe, and G. Volpe, “Active particles in complex and crowded environments,” *Rev. Mod. Phys.* **88**, 045006 (2016).
- [4] S. Palagi and P. Fischer, “Bioinspired microrobots,” *Nat. Rev. Mater.* **3**, 113–124 (2018).
- [5] D. M. Woolley, R. F. Crockett, W. D. I. Groom, and S. G. Revell, “A study of synchronisation between the flagella of bull spermatozoa, with related observations,” *J. Exp. Biol.* **212**, 2215–2223 (2009).
- [6] Y. Yang, J. Elgeti, and G. Gompper, “Cooperation of sperm in two dimensions: synchronization, attraction, and aggregation through hydrodynamic interactions,” *Phys. Rev. E* **78**, 061903 (2008).
- [7] R. Nosrati, A. Driouchi, C. M. Yip, and D. Sinton, “Two-dimensional slither swimming of sperm within a micrometre of a surface,” *Nat. Comm.* **6**, 8703 (2015).
- [8] M.-J. Kim, J. C. Bird, A. J. Van Parys, K. S. Breuer, and T. R. Powers, “A macroscopic scale model of bacterial flagellar bundling,” *Proc. Natl. Acad. Sci. USA* **100**, 15481–15485 (2003).
- [9] S. Y. Reigh, R. G. Winkler, and G. Gompper, “Synchronization and bundling of anchored bacterial flagella,” *Soft Matter* **8**, 4363–4372 (2012).
- [10] D. R. Brumley, M. Polin, T. J. Pedley, and R. E. Goldstein, “Hydrodynamic synchronization and metachronal waves on the surface of the colonial alga *Volvox carteri*,” *Phys. Rev. Lett.* **109**, 268102 (2012).
- [11] J. Elgeti and G. Gompper, “Emergence of metachronal waves in cilia arrays,” *Proc. Natl. Acad. Sci. USA* **110**, 4470–4475 (2013).
- [12] G. I. Taylor, “Analysis of the swimming of microscopic organisms,” *Proc. R. Soc. Lond. A* **209**, 447–461 (1951).
- [13] D. R. Brumley, K. Y. Wan, M. Polin, and R. E. Goldstein, “Flagellar synchronization through direct hydrodynamic interactions,” *eLife* **3**, e02750 (2014).
- [14] T. J. Pedley and J. O. Kessler, “Hydrodynamic phenomena in suspensions of swimming microorganisms,” *Annu. Rev. Fluid Mech.* **24**, 313–358 (1992).
- [15] R. Golestanian, J. M. Yeomans, and N. Uchida, “Hydrodynamic synchronization at low Reynolds number,” *Soft Matter* **7**, 3074–3082 (2011).
- [16] A. J. Reynolds, “The swimming of minute organisms,” *J. Fluid Mech.* **23**, 241–260 (1965).
- [17] E. O. Tuck, “A note on a swimming problem,” *J. Fluid Mech.* **31**, 305–308 (1968).
- [18] E. Diller, J. Zhuang, G. Z. Lum, M. R. Edwards, and M. Sitti, “Continuously distributed magnetization profile for millimeter-scale elastomeric undulatory swimming,” *Appl. Phys. Lett.* **104**, 174101 (2014).
- [19] H.-W. Huang, M. S. Sakar, A. J. Petruska, S. Pané, and B. J. Nelson, “Soft micromachines with programmable motility and morphology,” *Nat. Comm.* **7**, 12263 (2016).
- [20] G. J. Elfring and E. Lauga, “Hydrodynamic phase locking of swimming microorganisms,” *Phys. Rev. Lett.* **103**, 088101 (2009).
- [21] B. Friedrich, “Hydrodynamic synchronization of flagellar oscillators,” *Eur. Phys. J. Special Topics* **225**, 2353–2368 (2016).
- [22] G. J. Elfring and E. Lauga, “Passive hydrodynamic synchronization of two-dimensional swimming cells,” *Phys. Fluids* **23**, 011902 (2011).
- [23] L. J. Fauci, “Interaction of oscillating filaments: a computational study,” *J. Comp. Phys.* **86**, 294–313 (1990).
- [24] L. J. Fauci and A. McDonald, “Sperm motility in the presence of boundaries,” *Bull. Math. Biol.* **57**, 679–699 (1995).
- [25] M. Theers and R. G. Winkler, “Synchronization of rigid microrotors by time-dependent hydrodynamic interactions,” *Phys. Rev. E* **88**, 023012 (2013).
- [26] G. J. Elfring and E. Lauga, “Synchronization of flexible sheets,” *J. Fluid Mech.* **674**, 163–173 (2011).
- [27] G. J. Elfring, O. S. Pak, and E. Lauga, “Two-dimensional flagellar synchronization in viscoelastic fluids,” *J. Fluid Mech.* **646**, 505–515 (2010).
- [28] J. C. Crispell, L. J. Fauci, and M. Shelley, “An actuated elastic sheet interacting with passive and active structures in a viscoelastic fluid,” *Phys. Fluids* **25**, 013103 (2013).
- [29] C.-K. Tung, C. Lin, B. Harvey, A. G. Fiore, F. Ardon, M. Wu, and S. S. Suarez, “Fluid viscoelasticity promotes collective swimming of sperm,” *Sci. Rep.* **7**, 3152 (2017).
- [30] P. Español and M. Revenga, “Smoothed dissipative particle dynamics,” *Phys. Rev. E* **67**, 026705 (2003).
- [31] K. Müller, D. A. Fedosov, and G. Gompper, “Smoothed dissipative particle dynamics with angular momentum conservation,” *J. Comp. Phys.* **281**, 301–315 (2015).

- [32] A. Vázquez-Quesada, M. Ellero, and P. Español, “Smoothed particle hydrodynamic model for viscoelastic fluids with thermal fluctuations,” *Phys. Rev. E* **79**, 056707 (2009).
- [33] J. J. Monaghan, “Smoothed particle hydrodynamics,” *Annu. Rev. Astron. Astrophys.* **30**, 543–574 (1992).
- [34] P. J. Hoogerbrugge and J. M. V. A. Koelman, “Simulating microscopic hydrodynamic phenomena with dissipative particle dynamics,” *Europhys. Lett.* **19**, 155–160 (1992).
- [35] P. Español and P. Warren, “Statistical mechanics of dissipative particle dynamics,” *Europhys. Lett.* **30**, 191–196 (1995).
- [36] X. Y. Hu and N. A. Adams, “Angular-momentum conservative smoothed particle dynamics for incompressible viscous flows,” *Phys. Fluids* **18**, 101702 (2006).
- [37] I. O. Götze, H. Noguchi, and G. Gompper, “Relevance of angular momentum conservation in mesoscale hydrodynamics simulations,” *Phys. Rev. E* **76**, 046705 (2007).
- [38] M. P. Allen and D. J. Tildesley, *Computer simulation of liquids* (Clarendon Press, New York, 1991).
- [39] L. B. Lucy, “A numerical approach to the testing the fission hypothesis,” *Astronom. J.* **82**, 1013–1024 (1977).
- [40] J. P. Morris, P. J. Fox, and Y. Zhu, “Modeling low Reynolds number incompressible flows using SPH,” *J. Comp. Phys.* **136**, 214–226 (1997).
- [41] L. D. G. Sigalotti, J. Klapp, E. Sira, Y. Meleán, and A. Hasmy, “SPH simulations of time-dependent Poiseuille flow at low Reynolds numbers,” *J. Comp. Phys.* **191**, 622–638 (2003).
- [42] M. Meister, G. Burger, and W. Rauch, “On the Reynolds number sensitivity of smoothed particle hydrodynamics,” *J. Hydraul. Res.* **52**, 824–835 (2014).
- [43] E. Lauga, “Propulsion in a viscoelastic fluid,” *Phys. Fluids* **19**, 083104 (2007).
- [44] E. A. Gaffney, H. Gadêlha, D. J. Smith, J. R. Blake, and J. C. Kirkman-Brown, “Mammalian sperm motility: observation and theory,” *Annu. Rev. Fluid Mech.* **43**, 501–528 (2011).
- [45] G. Saggiorato, L. Alvarez, J. F. Jikeli, U. B. Kaupp, G. Gompper, and J. Elgeti, “Human sperm steer with second harmonics of the flagellar beat,” *Nat. Comm.* **8**, 1415 (2017).
- [46] R. Adler, “A study of locking phenomena in oscillators,” *Proc. IRE* **34**, 351–357 (1946).
- [47] T. Niedermayer, B. Eckhardt, and P. Lenz, “Synchronization, phase locking, and metachronal wave formation in ciliary chains,” *Chaos* **18**, 037128 (2008).
- [48] K. Ishimoto and E. A. Gaffney, “Hydrodynamic clustering of human sperm in viscoelastic fluids,” *Sci. Rep.* **8**, 15600 (2018).
- [49] M. Sauzade, G. J. Elfring, and E. Lauga, “Taylor’s swimming sheet: analysis and improvement of the perturbation series,” *Physica D* **240**, 1567–1573 (2011).
- [50] Jülich Supercomputing Centre, “JURECA: Modular supercomputer at Jülich Supercomputing Centre,” *J. Large-Scale Res. Facil.* **4**, A132 (2018).